

Nanoscale

Accepted Manuscript



This is an *Accepted Manuscript*, which has been through the Royal Society of Chemistry peer review process and has been accepted for publication.

Accepted Manuscripts are published online shortly after acceptance, before technical editing, formatting and proof reading. Using this free service, authors can make their results available to the community, in citable form, before we publish the edited article. We will replace this *Accepted Manuscript* with the edited and formatted *Advance Article* as soon as it is available.

You can find more information about *Accepted Manuscripts* in the [Information for Authors](#).

Please note that technical editing may introduce minor changes to the text and/or graphics, which may alter content. The journal's standard [Terms & Conditions](#) and the [Ethical guidelines](#) still apply. In no event shall the Royal Society of Chemistry be held responsible for any errors or omissions in this *Accepted Manuscript* or any consequences arising from the use of any information it contains.



Journal Name

ARTICLE

Diversity of Sub-Bandgap States in Lead-Sulfide Nanocrystals: Real-Space Spectroscopy and Mapping at the Atomic-Scale

Christian F. Gervasi,^a Dmitry A. Kislitsyn,^a Thomas L. Allen,^b Jason D. Hackley,^{a,‡} Ryuichiro Maruyama,^{a,§} and George V. Nazin^a

Received 00th January 20xx,
Accepted 00th January 20xx

DOI: 10.1039/x0xx00000x

www.rsc.org/

Colloidal semiconductor nanocrystals have emerged as a promising class of technological materials with optoelectronic properties controllable through quantum-confinement effects. Despite recent successes in this field, an important factor that remains difficult to control is the impact of the nanocrystal surface structure on the photophysics and electronic transport in nanocrystal-based materials. In particular, the presence of surface defects and irregularities can result in the formation of localized sub-bandgap states that can dramatically affect the dynamics of charge carriers and electronic excitations. Here we use Scanning Tunneling Spectroscopy (STS) to investigate, in real space, sub-bandgap states in individual ligand-free PbS nanocrystals. In the majority of studied PbS nanocrystals, spatial mapping of electronic density of states with STS shows atomic-scale variations attributable to the presence of surface reconstructions. STS spectra show that the presence of surface reconstructions results in formation of surface-bound sub-bandgap electronic states. The nature of the surface reconstruction varies depending on the surface stoichiometry, with lead-rich surfaces producing unoccupied sub-bandgap states, and sulfur-rich areas producing occupied sub-bandgap states. Highly off-stoichiometric areas produce both occupied and unoccupied states showing dramatically reduced bandgaps. Different reconstruction patterns associated with specific crystallographic directions are also found for different nanocrystals. This study provides insight into the mechanisms of sub-bandgap state formation that, in a modified form, are likely to be applicable to ligand-passivated nanocrystal surfaces, where steric hindrance between ligands can result in under-coordination of surface atoms.

1 Introduction

Tunable thin-film structures formed from lead-chalcogenide (PbX, where X=S, Se or Te) nanocrystals (NCs) are a promising class of semiconducting materials with a combination of unique functionalities that makes them highly attractive for a new generation of optoelectronic applications.¹⁻⁴ Some of these functionalities are made possible by the ultra-small size of NCs, with such examples as greatly increased efficiencies for exciton-multiplication,⁵⁻¹⁰ and enhanced extraction of unrelaxed hot charge-carriers.¹¹ Another important functionality of NCs is the tunability of their properties via synthetic means, which allows one to systematically control the electronic bandgap by tuning the NC size. Additional

means of control, to improve the injection and extraction of charge carriers in PbX NC thin films, have been implemented through post-synthesis techniques¹² involving ligand exchange.¹³⁻¹⁵ Thus processed PbSe NC thin films show significantly reduced inter-particle spacings and dramatically increased conductivities.¹⁶⁻¹⁸ Less commonly, thermal annealing of the NC films is used,^{15, 16, 19, 20} which can result in extensive rearrangements of ligand shells as well as (at higher temperatures) sintering²¹ and even fusion^{22, 23} of NCs. These processing steps, necessary for achieving optimal charge transport properties in NC films, simultaneously present significant challenges because they tend to radically alter the surface chemistry of NCs, with the potential to create surface imperfections that can result in the appearance of sub-bandgap trap states, which, in turn, have a strong impact on charge-carrier dynamics, recombination, and extraction from NC films.²⁴⁻²⁶

Indeed, recent breakthroughs in increasing the efficiency of PbX NC-based photovoltaic devices were made possible, to a great extent, by developments in surface passivation techniques that enabled a significant reduction in the density of surface trap states,^{27, 28} with some of the reported efficiencies exceeding ~8%.^{29, 30} Some of the promising approaches have employed passivation with mercaptopropionic acid,³¹ atomic passivation with halogens,

^a Department of Chemistry and Biochemistry, Materials Science Institute, University of Oregon, 1253 University of Oregon, Eugene, Oregon 97403, United States.

^b VoxelNano, a division of Voxel, Inc, CAMCOR/Lorry Lokey Labs, 1241 University of Oregon, Eugene, OR 97403-1241, United States.

[†] Electronic Supplementary Information (ESI) available: Additional examples of PbS NCs displaying localized defect-related states and dI/dV intensity maps of NC2 exhibiting anti-correlation behaviour of defect states are shown. See DOI: 10.1039/x0xx00000x

[‡] Current address: Intel Corp., 2501 NW 229th Avenue, Hillsboro, OR 97124

[§] Current address: New Energy and Industrial Technology Development Organization (NEDO), 18F Muza Kawasaki Central Tower, 1310 Omiya-cho, Saiwai-ku, Kawasaki City, Kanagawa 212-8554 Japan

ions and SCN⁻,^{25, 32} and inorganic ligands,³³ metal halide and chalcogenide salts,^{18, 34} amorphous alumina,¹⁸ and alkylselenide ligands.³⁵ Conceptually, complete elimination of trap states requires consideration of the “passivating effect” of individual surface ligands, and careful balancing of the number of ligands with the NC core stoichiometry, a difficult task in practice. In particular, theoretical calculations show that in the limiting case of ligand-free stoichiometric NCs, midgap states do not exist,^{36, 37} but in non-stoichiometric Pb-rich (Pb-poor) NCs sub-bandgap states are found near the conduction (valence) bands.^{36, 38} A similar picture holds for ligand-passivated NCs: attachment of ligands effectively changes NC stoichiometry, such that an appropriate number of ligands can effectively compensate for the non-stoichiometry of the NC core, and eliminate the sub-bandgap states.³⁸ The importance of NC stoichiometry in defining the NC electronic structure is corroborated by recent experimental studies where the trap state densities were found to be sensitive to controlled variations in NC stoichiometry achieved either through post-synthesis ligand exchange,³⁵ direct thermal deposition,³⁹ solution-based colloidal atomic layer deposition,⁴⁰ and successive ionic layer adsorption and reaction (SILAR).⁴¹

Optimization of the “effective” NC stoichiometry is complicated by the varied chemistry of facets associated with different crystallographic directions (typically {111}, {100} and, to a lesser extent, {110})⁴².³⁵ A stark manifestation of this variability is the fact that unlike stable {110} and {100} surfaces,^{43, 44} (unpassivated) polar {111} surfaces are unstable and are predicted to undergo reconstruction resulting in formation of an ordered sub-monolayer of Pb atoms.⁴⁵ Evidence for surface reconstruction is provided by Rutherford backscattering experiments on PbSe thin films, where a sub-monolayer (~40%) of Pb atoms, consistent with surface reconstruction, was found.⁴⁶ Additional evidence was provided by TEM imaging of PbSe NC {111} facets showing ribbon-like Pb structures attributed to surface reconstruction.⁴⁵

While considerable advances in controlling the properties of PbX NC films have been made, and several theoretical studies showing the importance of surface trap states are available,^{25, 38, 47} the role of surface trap states in the physical picture of charge-carrier photo-generation and dynamics remains to be fully addressed. Experimental studies of surface trap states have been carried out using a variety of techniques. Photoluminescence studies showed the existence of trap states in as-synthesized ligand-passivated PbX NCs,^{48, 49} even before NC film formation. Photoluminescence measurements of ligand-exchanged PbX NC films demonstrated the presence of trap states^{31, 50} that could be manipulated with NC size and surface treatment.^{31, 49} Trap states in ligand-exchanged PbX NCs were also found in studies utilizing deep-level transient and Fourier-transform photocurrent spectroscopies,⁵¹ and in spectroscopic measurements of photocurrent in PbS field-effect transistor devices.⁵² Even though these studies have provided rich insights into the spectroscopic properties of surface trap states, they lacked the spatial resolution to visualize the relationship between the local structure of NC surfaces and properties of such states. The capability to probe

this relationship is critically important for the development of a microscopic picture of surface trap states because of the wide diversity of local atomic-scale surface structures associated with variations in ligand-shell morphologies, the presence of different crystallographic facets, NC shape variations, and the effect of surface reconstruction.

A direct spectroscopic approach for real-space investigations of surface states in individual NCs is afforded by a combination of Scanning Tunneling Microscopy (STM) and Scanning Tunneling Spectroscopy (STS), which have been used to probe the electronic states in ligand-exchanged PbS NC films.^{53, 54} Realization of this technique in a high-stability cryogenic STM system⁵⁵ enables detailed atomic-scale mapping of electronic states in individual NCs. STS-based mapping of the local density of states (DOS) was recently used to study the spatial localization and spectral properties of sub-bandgap states in NCs arising due to local off-stoichiometry.⁵⁶ Here we apply this experimental approach to obtain *atomic-scale* DOS maps of individual ligand-free PbS NCs. Ligand-free NCs represent a well-defined model PbX system, unaffected by the uncontrolled variances of the ligand shell morphology, which makes this system more open to theoretical simulations.^{44, 57, 58} STS maps show that the majority of studied NC surfaces underwent reconstruction accompanied by formation of ordered atomic patterns commensurate with the crystallographic structures of the NC surfaces. While these results are in accordance with density-functional theory calculations of polar PbS surfaces, where similar modes of surface reconstruction were predicted,⁴⁵ the current manuscript reports, for the first time, results demonstrating the connection between the atomic-scale NC surface morphology and atomic-scale variations in the electronic DOS. Importantly, we find that NC surface reconstruction results in formation of surface-bound sub-bandgap electronic states with spectral and spatial properties sensitive to the local stoichiometry of NC surfaces. In addition, we find that highly off-stoichiometric NC regions show qualitatively different defect states with energies deep inside the NC bandgaps. By employing results of calculations for off-stoichiometric PbX NCs,³⁸ we infer the presence of off-stoichiometric areas from local DOS spectra, and use DOS maps to analyze the local spatial variations in stoichiometry.

2 Experimental Methods

A Au(111) substrate surface was prepared, under ultra-high vacuum conditions ($\sim 10^{-11}$ Torr), by several cycles of sputtering/annealing, using Ne gas, and annealed at $\sim 400^\circ\text{C}$. Pentanethiol-terminated PbS NCs were synthesized as described previously,⁵⁶ suspended in pentane, and deposited onto the Au(111) surface using a solenoid pulse-valve. During deposition, the Au(111) substrate was held inside the load-lock section of the vacuum system, with the pressure not exceeding 10^{-6} Torr during deposition. Several successive bursts of the solenoid valve were used to obtain a sub-monolayer of PbS NCs on the Au(111) surface. The Au(111) substrate with deposited NCs was annealed in ultra-high vacuum conditions

at increasingly higher temperatures until well-defined reproducible STM imaging of individual NCs was achieved, with a final annealing temperature of $\sim 170^\circ\text{C}$.

Experiments were conducted using a home-built ultra-high-vacuum STM incorporating a Pan-type scanner provided by RHK Technology.⁵⁵ All STS spectra were recorded using a lock-in amplifier operating at a modulation frequency of ~ 600 Hz, and bias voltage modulation varying from ~ 10 mV (for individual spectra and one-dimensional spatial DOS maps) to ~ 50 mV (for two-dimensional DOS maps). All STM images and STS spectra were obtained at a temperature of ~ 15 K with electrochemically etched Ag tips.

3 Results and Discussion

3.1 Sample preparation

PbS NCs with pentane-thiol ligand shells were deposited on Au(111) surfaces and annealed at progressively higher temperatures until ligands were removed. The removal of ligands was monitored with STM imaging, which, at the initial stages of annealing, typically showed fuzzy patterns consistent with dynamic reorientation of ligands present on the NC surface (Figures 1a-c). At the final stages of annealing, the majority of NCs showed reproducible topographic patterns suggesting the absence of ligand reorientation (Figures 1d-f). In addition, STM images of fully-annealed NCs showed disc-like width-to-height aspect ratios of 2:1 to 3:1 suggesting that significant reconstruction of the overall shapes of NCs occurred during the annealing process. The disc-like shapes of

annealed NCs are consistent with similar shapes of PbS and PbSe NCs grown by electrodeposition on Au(111).^{59, 60} The predominance of disc-like shapes in a polar material like PbS, attributable to the reduced electrostatic NC energy (due to screening by the gold surface) enabled by this geometry. Importantly, images of fully-annealed NCs often showed surface features aligned at specific angles attributable to well-defined crystallographic directions in PbS NCs (Figures 1g-i). The majority of fully-annealed NCs showed topographic features (e.g. NC boundaries and topographic steps) oriented along three main spatial directions (specific to each NC), forming 120° angles with respect to each other (Figures 1g and h), even though other orientations have also been observed (Figure 1i). The existence of such directional order suggests that the top-most NC surfaces (in most cases) roughly correspond to $\{111\}$ crystallographic surfaces, consistent with results of TEM studies of PbS NCs terminated with Au clusters,⁶¹ where the polar nature of the $\{111\}$ facets was reported to lead to preferential formation of Au/PbS $\{111\}$ interfaces. Results described in the following summarize our studies of 10 fully-annealed individual PbS NCs.

3.2 DOS-spectroscopy of NCs

Energy-dependent DOS spectra (STS spectra) of individual PbS NCs were recorded by measuring the differential tunneling conductance, dI/dV , as a function of the bias voltage (see Methods for details of the measurements).⁶² DOS spectra for all fully-annealed NCs show progressions of peaks associated with occupied (negative bias) and unoccupied (positive bias) electronic states (Figure 2a). Indeed, while Figure 2a shows considerable variations in the apparent band gaps ($E_{1,1} - E_{1,2}$ energy difference) for different NCs, the DOS spectra, overall, appear quite similar and reminiscent of those calculated for stoichiometric ligand-free PbX NCs,^{44, 57, 58} where the electronic states can be described as quantum-confined particle-in-a-box (PIAB) states originating from the conduction and valence bands. The lowest-energy PIAB states are predicted to show s- and p- overall orbital symmetries, with their atomic-scale behavior determined by the corresponding Bloch wavefunctions.⁵⁷ A similar picture of PIAB-like electronic states has been used to describe STS spectra for a variety of NCs composed of different semiconductor materials.⁶³ Then, taking into account the disk-like aspect ratio of studied NCs, the unoccupied states in Figure 2a could be assigned in the following way: the doublet of closely spaced peaks $E_{1,1}$ and $E_{1,2}$ may be attributed to electronic states quantized in the X-plane (with $E_{1,1}$ being the ground state), whereas the E_2 state may be attributed to a single-node state quantized in the Z-direction.⁵⁹ By using the PIAB-like picture of electronic states in Figure 2a, the variations in the apparent bandgap ($E_{1,1} - E_{1,2}$ energy difference) could then potentially be explained by variations in NC dimensions, which would modulate the energies of the PIAB states via quantum-size effects.⁶⁴

The PIAB-like picture of electronic states in Figure 2a is challenged, however, by the fact that the spacing between peaks $E_{1,1}$ and $E_{1,2}$ does not change appreciably from one NC to

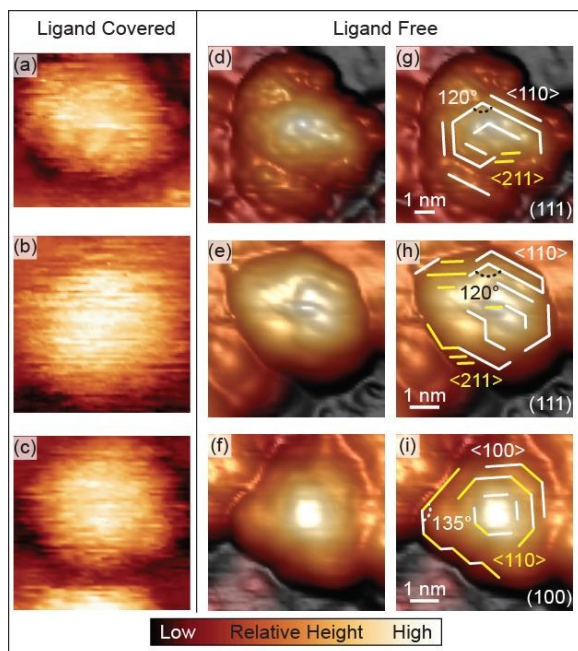


Fig. 1 STM topographies of ligand-covered (a)-(c) and ligand-free (d)-(f) PbS NCs. Figures (g)-(i) highlight topographical features observed in (d)-(f). The crystallographic directions and NC boundaries are identified with the aid of STS DOS mapping. All STM topographies measured with set-point 2.0 V bias, 1-2 pA tunnelling current.

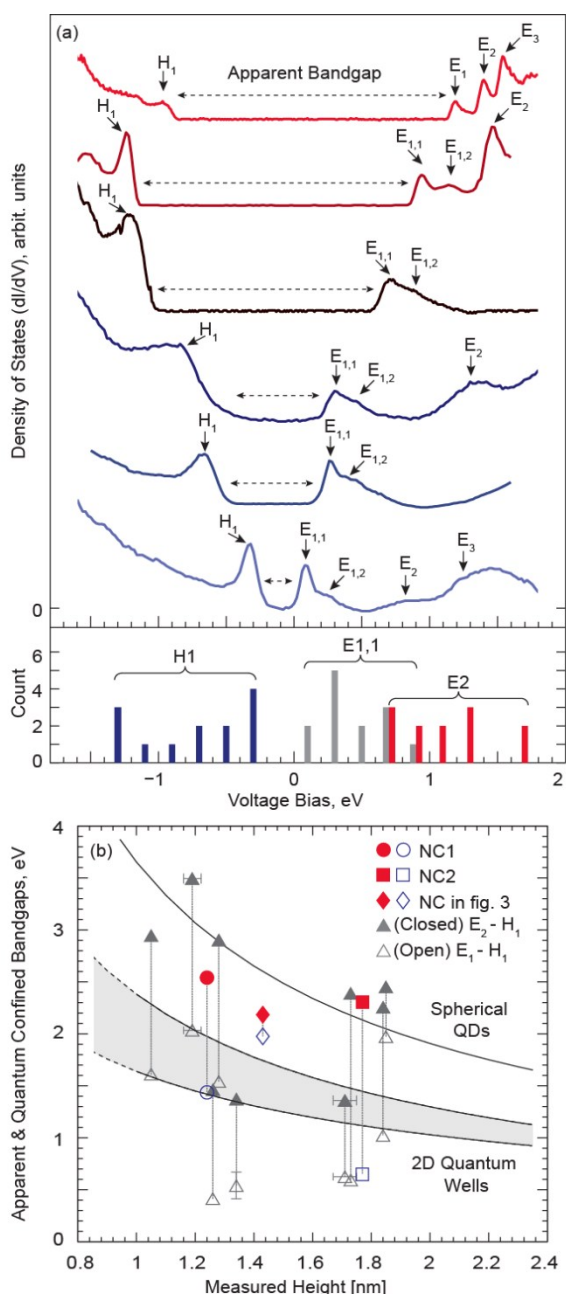


Fig. 2 (a) DOS spectra for six representative PbS NCs (individual spectra shifted for clarity). Occupied (unoccupied) states denoted by H_n (E_n) respectively. All dI/dV curves measured with set-point 1.6–2.6 V bias, 15–30 pA tunnelling current. Histogram (bottom) of energetic locations and distributions for discernible states $E_{1,1}$, E_2 , and H_1 for 13 NCs, bin size 0.2 eV (b) Bandgaps vs. height for measured NCs overlaid on data for two limiting cases: spherical NCs and 2D PbS quantum wells. Open symbols correspond to the $E_{1,1} - H_1$ energy differences, whereas closed symbols correspond to values obtained from PIAB orbitals differences of many measured DOS spectra in Figure 2a are considerably lower than those (as determined from DOS mapping). The curve for spherical PbS NCs, and gray shaded region corresponding to 2D PbS quantum wells, were obtained from Moreels et al.⁶⁵ and Lee et al.,⁶⁶ respectively.

another, being consistently in the range of ~ 0.2 eV despite significant variations in the NC lateral sizes. Further, the apparent bandgaps ($E_{1,1} - H_1$) energy expected based on the physical dimensions of the corresponding NCs. Indeed, many of the apparent bandgaps are lower than what would be

expected for two-dimensional PbS films of thicknesses matching the observed NC heights (Figure 2b),⁶⁷ which is the absolute minimum expected for NCs with large spatial dimensions in the XY plane. On the other hand, energy differences calculated from $E_2 - H_1$ (and in some cases $E_2 - H_1$) tend to fall in the range expected for bandgaps of disc-like PbS NCs (Figure 2b). Together, these observations suggest that E_n states in Figure 2a do not have PIAB-like character, and may potentially be associated with sub-bandgap states. Theoretical calculations predict that sub-bandgap states are often more strongly localized than PIAB-like states derived from the conduction and valence bands,^{38, 47} which suggests that to establish the nature of electronic states observed in Figure 2a, it would be useful to obtain information regarding their spatial behavior. To this end, we carried out spatial mapping of DOS spectra for several NCs, as described below.

3.3 Surface-Reconstruction observed in DOS maps: Results

We first present DOS maps for NCs that showed E_n states delocalized over the NC surfaces. For example, Figure 3 shows a “cross-sectional” DOS mapping for a NC without apparent spectral or spatial features attributable to sub-bandgap states. Indeed, the apparent bandgap of this NC falls within the range expected for disc-like NCs (Figure 2a, diamond-shaped data point), unlike the majority of studied NCs. The DOS map (Figure 3b) is composed of a progression of DOS spectra measured across the NC, as shown in Figure 3a. In Figure 3b, occupied state H_1 and all unoccupied states E_n are visible throughout the scan (even though they also show some variations in their intensities), which suggests that they may correspond to delocalized PIAB-like states.

While delocalized states analogous to those of Figure 3b were observed for many other NCs, their maps were often different from that of Figure 3b in that they showed quasi-periodic spatial modulations of their DOS intensities. An example of a “cross-sectional” DOS map for one such NC (referred to as NC1 in the following) is shown in Figure 4. The DOS spectra measured at different locations on the NC1 surface show a similar grouping of occupied and unoccupied states with intensities modulated depending on the measurement location (Figures 4b and c). In particular, distinct modulations are observed for states H_1 , $E_{1,1}$ and $E_{1,2}$ (Figure 4b). These modulations occur on a spatial scale far exceeding the unit cell of PbS (0.59 nm), suggesting that they are not product of elemental contrast originating from the PbS lattice. The magnitudes of $E_{1,1} - H_1$ and $E_2 - H_1$ bandgaps for NC1 (Figure 2a, open and closed circle data-points) suggest the presence of sub-bandgap states.

To further investigate the spatial behavior of electronic states in NC1, we recorded DOS spectra across a two-dimensional grid of points covering (roughly) the spatial extent of NC1. 2D-spatial maps of electronic states are obtained from this DOS dataset by taking values of the DOS at select bias voltages. Such 2D-maps for the most prominent occupied and unoccupied states are shown in Figure 5 and in supplementary Figures S1 and S2. The 2D-spatial maps in Figure 5 show that individual states in NC1 have very different characters, exce-

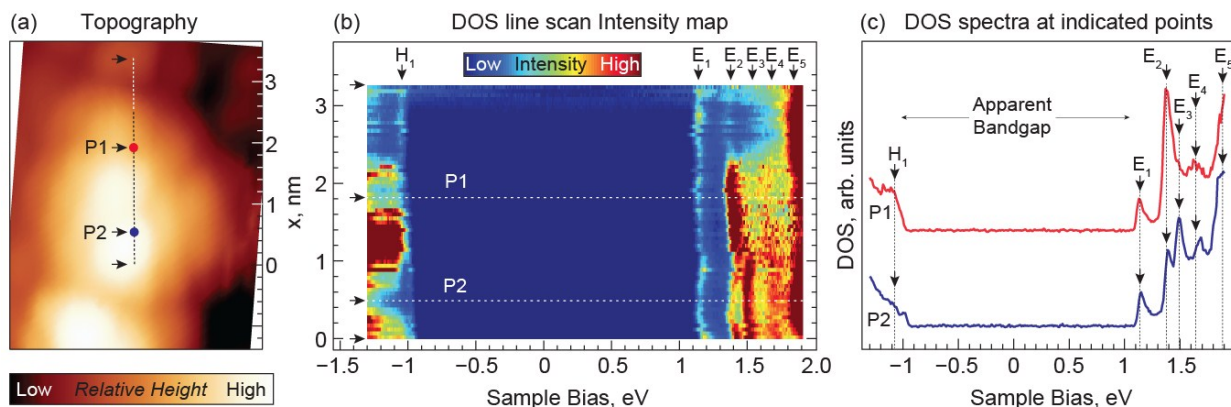


Figure 3 (a) STM topographic image of a PbS NC. (b) DOS "cross-section" mapping along the path of the dotted line in (a). (c) Individual DOS spectra measured at locations marked in (a). STS measurements in (b) and (c) were taken with a set-point of 1.9 V bias and 30 pA tunnelling current. Variations in the energies of electronic states across the NC roughly follow the NC topography, which is a result of the location-specific variation of the bias voltage drop inside the NC.⁵⁶

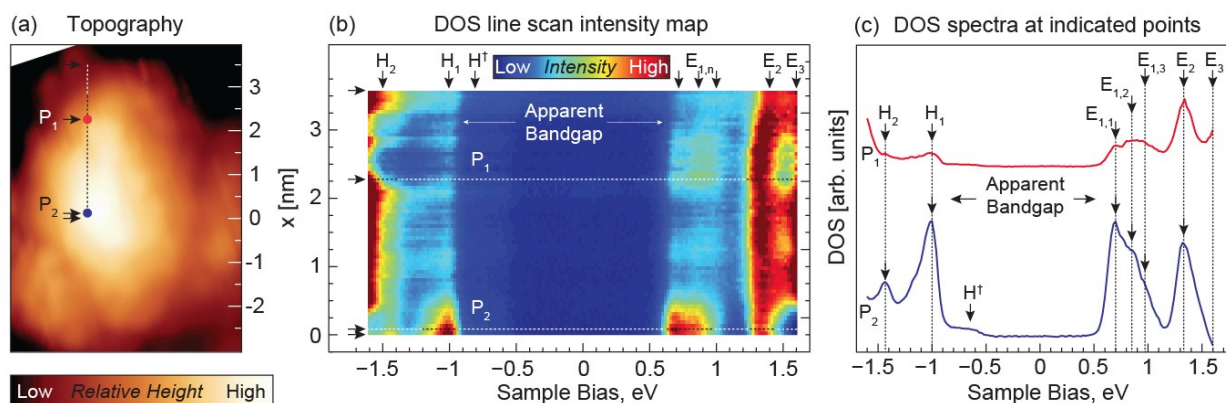


Fig. 4 (a) STM topographic image of NC1. (b) DOS mapping of NC1 along the path of the dotted line in (a). (c) Individual DOS spectra for locations marked in (a). STS measurements in (b) and (c) were taken with set-point 1.6 V bias, 30 pA tunnelling current.

in the $E_{1,n}$ states (Figures 5c, and S1c-e), as well as states H_1 and H_1^+ (Figures 5d,e; S2a,b), which exhibit similar features and spatial localizations respectively. All 2D DOS maps in Figure 5 show highly inhomogeneous spatial distributions with stripe-like "hot spots" oriented parallel to the $\langle 110 \rangle$ crystallographic features observed in the STM topography of NC1 (Figure 1g). For example, the DOS map of state E_3 (Figure 5a) shows two pairs of parallel bright "stripes" (marked with solid black lines in Figure 5a). The "stripes" in each pair are separated by distances equal to 0.726 nm , which is a close fit to the distance between atomic rows located in two different $\{211\}$ planes. In the following this distance is defined as 3α , where α is the distance between two neighboring $\{211\}$ planes, as shown in the model in Figures 6a and b. The two pairs of bright stripes in Figure 5a are separated by a distance of $0.968 \text{ nm} = 4\alpha$, which corresponds to the geometry shown in the model in Figure 6b, where, in contrast to the model in Figure 6a, one of the atomic rows is located in a different (lower) $\{111\}$ atomic plane. This geometry is consistent with the topography of NC1 (Figure 1d),

which shows atomic steps separating the regions with the two pairs of DOS stripes seen in Figure 5a. The DOS map of state E_2 (Figure 5b) shows somewhat less-developed structural order, but features aligned along the same set of black lines are visible.

In contrast, DOS maps of $E_{1,n}$ states (Figures 5c, and S1c-e) show a different set of bright DOS "stripes" (marked with black lines), which are however, separated by the same distance of $0.726 \text{ nm} = 3\alpha$ as found in Figure 5a. In addition, all of the DOS "stripes" in Figures 5c, and S1c-e are either parallel to, or are oriented at exactly 60° with respect to the DOS "stripes" from Figure 5a, which is consistent with the mutual orientation of two different sets of $\{211\}$ planes, as shown in the model in Figure 6a. This, together with the spacing of DOS "stripes" in maps of $E_{1,n}$ states, suggests that the latter have a similar relationship with the PbS crystallographic structure as features found in the maps of states E_3 and E_2 . Stripe-like features similar to those found in maps of $E_{1,n}$ states, are also observed for states H_1^+ and H_1 , (black lines in Figures 5d and e). The DC

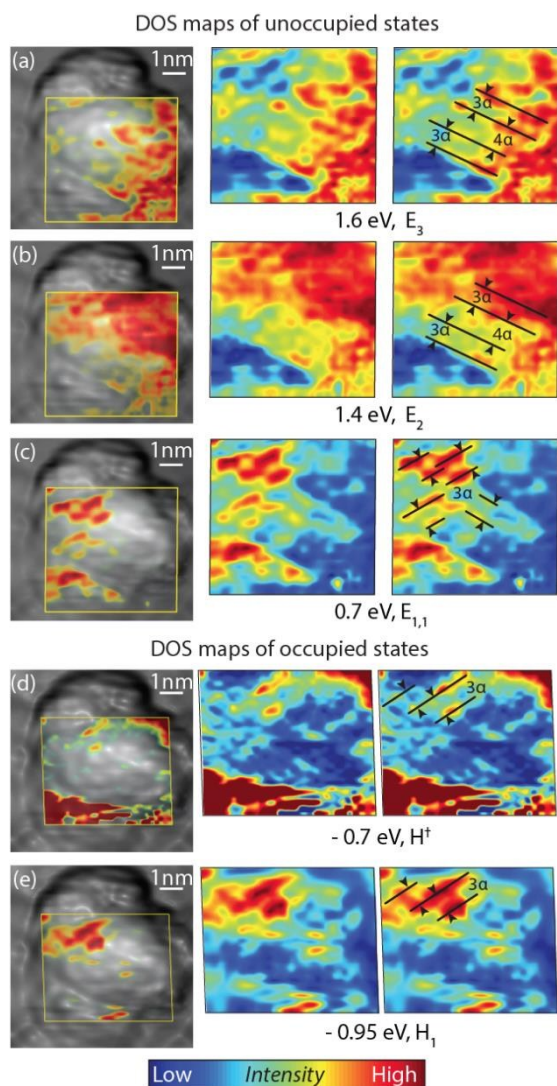


Fig. 5 2D DOS maps of unoccupied (a-c) and occupied (d, e) states for NC1. DOS state representations show (from left to right) combination topography/DOS map overlay (yellow outline indicates area of DOS mapping), DOS map only, and DOS map with black lines showing DOS features that are in registry with NC1 crystallographic features from Figure 1g. Parameter α is distance between two neighboring $\{211\}$ planes, as shown in the model in Figures 6a and b. STS measurements taken with set-point 1.6 V bias, 30 pA tunnelling current. STM topography image measured with set-point 2.0 V bias, 2 pA tunnelling current.

map of state H_2 (Figure S2c) shows somewhat less-developed order, with several features orthogonal to the bright $\{211\}$ plane features observed throughout (especially in Figures 5a,b) suggesting that they lie in $\{110\}$ planes of NC1. This assignment is supported by the fact that these features are separated by distances of ~ 0.838 nm = 4β , where β is a distance between two neighboring $\{110\}$ planes, as shown in Figures 6c and d.

The spatial order observed in the DOS maps of NC1 allows us to draw several conclusions. First, the fact that the orientations of bright DOS features in Figures 5, S1 and S2 are in registry with the crystallographic directions and lattice spacings expected for a $\{111\}$ surface, supports the conclusion (originally based on features observed in STM imaging – Figure

1g) that one of the $\{111\}$ crystallographic planes of NC1 is parallel to the Au(111) surface. By associating the DOS features with specific crystallographic directions, we are able to identify orientations of topographic features in Figure 1g as corresponding to different $\langle 110 \rangle$ directions. Further, the consistency of the spacing observed for these bright DOS features in all maps of Figure 5, S1 and S2 with the crystal structure of PbS suggests that these features are indeed associated with an atomic geometry analogous to that seen in the model of reconstructed PbS $\{111\}$ surfaces displayed in Figure 6, even though the actual morphology of NC1 is more complex.

3.4 Surface-Reconstruction: Discussion

The distances between the stripe-like features in Figures 5, S1 and S2 are larger than the minimal inter-atomic distance expected for the identified crystallographic directions. As the idealized model in figure 6 illustrates, this may result from a geometry where rows of atoms are missing on the PbS surface. Such surface morphology is consistent with the predicted reconstruction of the PbS(111) surface.⁴⁵ Indeed, the polar nature of PbS dictates that termination of a NC with a $\{111\}$ facet composed of only one element is electrostatically unfavorable. Instead, reconstruction of the PbS(111) surface is predicted, where, in the ideal case, a $\{111\}$ facet is stabilized by an additional ordered half-monolayer composed of the complementary element.⁴⁵ While different configurations of the additional half-monolayer are possible, one of the configurations that is predicted to give the lowest overall energy has a structure with atoms missing in every alternate $\{211\}$ plane, as shown in the model in Figure 6a. This structure results in rows of atoms oriented and spaced in a manner identical to the arrangement of bright rows in the DOS maps of NC1, which strongly suggests that the observed NC1 DOS features are caused by surface reconstruction.

To establish the composition of the reconstructed layer as well as the nature of electronic states in Figures 5, S1 and S2, we compare these results to theoretical predictions. Electronic structure calculations for unpassivated PbS NCs of different shapes show that in PbS, unoccupied states are primarily formed from atomic 6p-orbitals of lead, while occupied states are primarily formed from atomic 3p-orbitals of sulfur.⁴⁴ This distinction is maintained regardless of the NC shape and stoichiometry,³⁸ which is important for the case of NC1, since the model surface reconstruction shown in Figure 6a results in surface adatoms in non-stoichiometric environments. We thus expect that states $E_{1,n}$, E_2 and E_3 must be carried predominantly by surface Pb-atoms, whereas states H^+ , H_1 and H_2 must be carried predominantly by surface S-atoms. Moreover, non-stoichiometric Pb-atoms (or S-atoms), are predicted to form localized sub-bandgap states split-off from the conduction-band (or valence-band for S-atoms).³⁸ This prediction implies that since $E_{1,n}$ states are the lowest-energy unoccupied states, they must be associated with non-stoichiometric Pb-adatoms. The strong localization of $E_{1,n}$ “hot spots” along the specific crystallographic lines associated with reconstruction features further reinforces this assignment.

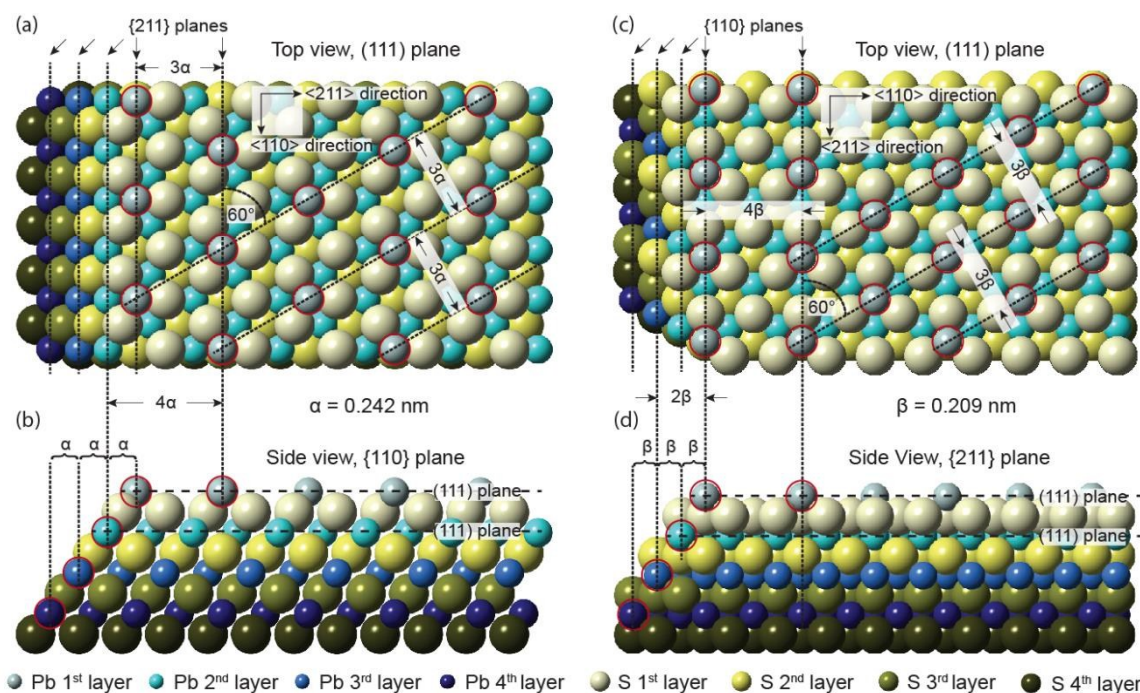


Fig. 6 Model representations of relevant PbS fcc crystallographic facets with idealized reconstruction features. (a, c) {111}-plane views showing rows of Pb adatoms oriented along $\langle 110 \rangle$ and $\langle 211 \rangle$ directions respectively, with indicated inter-atomic-row distances in integer multiples of distances α and β respectively. (b, d) {110}-, and {211}-plane side-view of same structures as in (a) and (c) showing vertical atomic steps responsible for appearance of varied distances between the bright DOS "stripes" in Figure 5 and Figure

In contrast, the high degree of delocalization of states E_2 and E_3 identifies them as quantum-confined PIAB states with spatial distributions modulated by the presence of the periodic surface structures formed from Pb-adatoms. Analogously, the spatial localization of states H^\dagger and H_1 suggests that they correspond to surface states produced by reconstruction, whereas state H_2 should correspond to a PIAB state. These assignments of the origins of the different NC1 states are supported by the fact that the NC1 bandgap calculated as $E_2 - H_2$ is in the correct range for a disk-like NC (determined from Figure 2b), unlike the apparent bandgap $E_{1,1} - H_1$, which is at the extreme low end of values corresponding to a 2D PbS thin film.

Identification of states $E_{1,n}$ as states carried by reconstructed Pb-adatoms allows us to address the existence of multiple peaks in the $E_{1,n}$ band, an observation that was common for most studied PbS NCs. Indeed, most of the DOS spectra measured on PbS NCs showed at least two $E_{1,n}$ states, separated in all spectra by roughly 200 mV (Figure 2a). This energetic separation is much larger than the typical vibrational energy scale of PbS,⁶⁸ which rules out current-induced vibrational excitation of NCs⁶⁹ as a potential cause for the appearance of multiple $E_{1,n}$ peaks. Instead, the existence of $E_{1,n}$ bands may be rationalized by considering adatom-adatom electronic coupling that has been shown to lead to formation of "bonding" and "anti-bonding" electronic states.⁴⁷ This interaction mechanism suggests a scenario analogous to that described in a number of recent STS studies of atomic structures similar to that exhibited in the model in Figure 6a,

where ordered rows of atoms adsorbed on surfaces with well-defined crystallographic order were investigated.⁷⁰⁻⁷² In these studies, formation of extended electronic states was qualitatively described using the linear-combination-of-atomic-orbitals (LCAO) model. By using this model, $E_{1,n}$ bands may be similarly attributed to LCAO-like electronic states formed from orbitals of under-coordinated Pb adatoms, such that individual $E_{1,n}$ states should correspond to distinctly different linear combinations of atomic orbitals. This physical picture not only explains the presence of multiple $E_{1,n}$ states, but also the close similarities in their 2D DOS maps (Figures 5c, S1c-e): because these states are formed from the same atomic orbitals, their linear combinations should only differ in their mutual phase and should produce the same spatial distributions.

3.5 NCs with Edge-Defects

While the delocalized $E_{1,n}$ states caused by surface reconstruction were found in almost all of the studied NCs, a *qualitatively different* type of sub-bandgap state attributable (as will be shown in the following) to surface defects was also observed in several NCs. DOS spectra showing these defect states for a representative NC (this NC is referred to as NC2 in the following) are shown in Figure 7. Unlike $E_{1,n}$ states, these defects exhibited a substantial DOS on the occupied side of the STS spectra (states H^\dagger , $H_{1,1}$ and $H_{1,2}$ in Figure 7), while defect-related DOS features appearing on the unoccupied side were often less pronounced (state E^\dagger in Figure 7) or absent (see Figure S5 for additional NCs showing similar defect-related states). In contrast to $E_{1,n}$ states, the defect states were tight

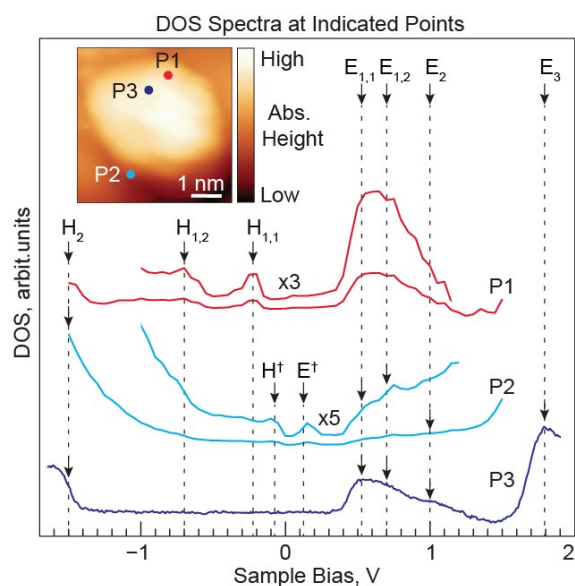


Fig. 7 DOS spectra for NC2 measured at locations P1-3 shown in the inset STM topography. Sections of spectra P1 and P2 containing relevant states have been magnified by designated amount for clarity. STS measurements were taken with set-points of 1.5-2.2 V bias, 10-20 pA tunnelling current. STM topography image measured with set-point 2.0 V bias, 1 pA tunneling current.

localized, as can be seen, for example, from the dramatic differences in DOS spectra measured in neighboring points P1 and P3 in Figure 7.

To visualize the entire spatial extents of these defect-states, we carried out 2D DOS mapping using the experimental approach described above for NC1. Maps of unoccupied states for NC2 (Figures 8a-c and S3) show a progression of $E_{1,n}$ and E_2 states analogous to that of NC1 (Figure 5), as well as state E^\dagger (Figure 8c). For NC2, however, the high-intensity DOS “stripes” of states $E_{1,n}$ and E_2 are oriented at an angle of 30° with respect to the NC2 edges, and exhibit spacings of $0.42 \text{ nm} = 2\beta$ and $0.63 \text{ nm} = 3\beta$ suggesting that these “stripes” are associated with a *different type* of surface reconstruction with atomic self-assembly along $\langle 211 \rangle$ directions, as shown by the atomic model in Figures 6c and d.

DOS maps of occupied states $H_{1,n}$ and H_2 (Figures 8d,e and S4b-d) show a progression analogous to that of $E_{1,n}$ and E_2 , except that DOS “stripes” in maps of $H_{1,n}$ show reconstruction along a $\langle 110 \rangle$ crystallographic direction. In addition, the nature of this reconstruction pattern is different from that of $E_{1,n}$ states: comparison of $H_{1,n}$ and $E_{1,n}$ maps for NC2 shows that these states are anti-correlated in intensity on the atomic scale (Figure S6), which suggests that $H_{1,n}$ and $E_{1,n}$ patterns are formed by atoms corresponding to different elements. As with NC1, $E_{1,n}$ states in NC2 should be primarily carried by Pb-atoms, which means that $H_{1,n}$ states should be carried by S-atoms. This conclusion is further strengthened by the results of theoretical calculations, which, in the absence of strong non-stoichiometry, predict that occupied states should be formed mainly from 3-p orbitals of sulfur atoms.³⁸

A spatial distribution that is dramatically different from previously considered reconstruction-induced states are found

for the lowest-energy unoccupied state E^\dagger (Figure 8c) and highest occupied state H^\dagger (Figure 8d), which are both strongly localized near the bottom-left boundary of NC2. States H_2 and $H_{1,2}$ are also strongly localized near the same part of the NC2 boundary, almost identically to the localization patterns of E^\dagger and H^\dagger , are also identifiable in all maps for the remaining occupied states (Figure 8d,e and S4a-d). The very small apparent bandgap (E^\dagger – H^\dagger) associated with these “boundary states”, together with the high degree of their spatial localization, suggests their defect-related origin. The spectral characteristics of these states are analogous to those obtained in model DFT simulations of highly off-stoichiometric PbS NCs.³⁸ As discussed earlier, in these calculations, excess of Pb (S) atoms leads to the appearance of split-off states below (above) the PIAB-like conduction (valence) band states. In highly off-stoichiometric

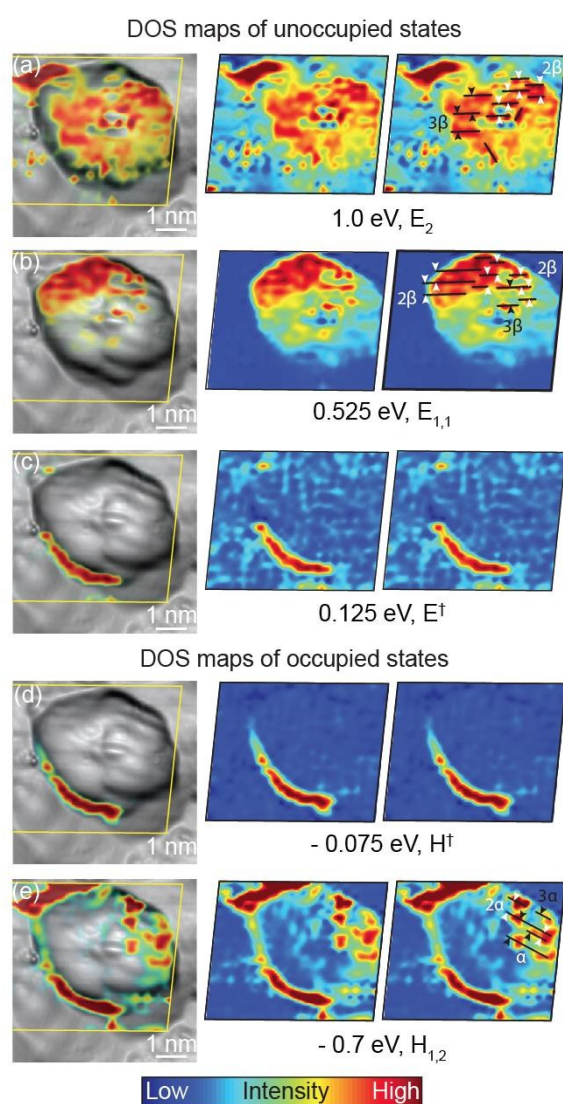


Fig. 8 Same as Figure 5 for NC2. Parameters α and β are the distances between two neighboring $\{211\}$ and $\{110\}$ planes respectively, as shown in the model in Figures 6. STM topography image measured with set-point 2.0 V bias, 1 pA tunnelling current. STS maps measured with set-point 1.5 V bias, 20 pA tunnelling current.

conditions, the energies of split-off states become sufficiently low (high) for them to appear on the occupied (unoccupied) side of DOS spectra. Thus, because with the exception of state E^+ , no other unoccupied "boundary states" are observed (Figures 8a,b), and, in contrast, "boundary states" are observed in maps of all occupied states, we associate the "boundary states" with sulfur-rich areas of NC2.

This assignment is consistent with the presence of extra sulfur atoms in the areas of states $H_{1,n}$, (top-right area of NC2 in Figures 8e and S4b,c), which are also localized near the NC2 boundaries: the near-boundary localization of states E^+ , H^+ and $H_{1,n}$ suggests that they could have been formed in a similar fashion, possibly due to migration of some of the Pb atoms to the Au(111) surface during annealing. Indeed, migration of Pb atoms to the Au substrate appears necessary to explain the existence of sulfur-rich areas, since as-synthesized PbS NCs are known to have Pb-rich surfaces.^{65, 73}

Conclusions

Our results show that reconstruction of polar PbS surfaces can produce a wide variety of sub-bandgap states with spatial structures and energies sensitive to the local stoichiometry. Both unoccupied and occupied trap states can be created in Pb-rich and S-rich areas, correspondingly. Wide bands of trap states crossing over the Fermi level can also exist in areas with sufficient local off-stoichiometry. The fact that the $E_{1,n}$ states were observed in the majority of fully annealed NC DOS suggests that most of these NCs underwent surface reconstruction. Indeed, one can expect this behavior to be common for ligand-free NCs, since their surfaces are likely to terminate with (111) facets, which are prone to reconstruction due to their polar nature.⁴⁵ This is consistent with DFT calculations, which show that unreconstructed (111) facets, are, in fact, unstable, and stability is only obtained for non-polar reconstructed facets.⁴⁵ In contrast, other facets corresponding to main crystallographic directions (100) and (110) are stable in their unreconstructed forms.⁴⁵

The presented results are directly applicable to thermally-processed NC solids, where loss of ligands is likely. Similar structure-dependent effects in the local DOS can also be expected for under-stoichiometric surfaces of ligand-passivated PbX NCs, where ligand self-assembly at the PbX-ligand interface may proceed with formation of surface-bound sub-bandgap states, as also suggested by calculations for CdSe NCs.^{74, 75} The STS-based characterization approach demonstrated in the present manuscript is applicable to NCs passivated with atomic-ligands,³² where similar questions of surface adatom self-assembly and resulting electronic structure need to be addressed.

Acknowledgements

This work was supported in part by the SONY Corporation. PbS NCs were supplied by VoxelNano. The STM instrument used in this work was constructed with support from the U.S. National

Science Foundation under Grant DMR-0960211. J.D.H. and G.V.N. acknowledge support from the NSF Center for Sustainable Materials Chemistry, grant CHE-1102637. STM images were processed using WSxM Software.⁷⁶

References

- 1 S. A. McDonald, G. Konstantatos, S. G. Zhang, P. W. Cyr, E. J. D. Klem, L. Levina and E. H. Sargent, *Nat. Mater.*, 2005, **4**, 131-136.
- 2 J. Tang, H. Liu, D. Zhitomirsky, S. Hoogland, X. H. Wang, M. Furukawa, L. Levina and E. H. Sargent, *Nano Lett.*, 2012, **12**, 4889-4894.
- 3 E. J. D. Klem, D. D. MacNeil, P. W. Cyr, L. Levina and E. H. Sargent, *Appl. Phys. Lett.*, 2007, **90**, 183113.
- 4 L. Sun, J. J. Choi, D. Stachnik, A. C. Bartnik, B.-R. Hyun, G. C. Malliaras, T. Hanrath and F. W. Wise, *Nat. Nanotechnol.*, 2012, **7**, 369-373.
- 5 A. J. Nozik, *Annu. Rev. Phys. Chem.*, 2001, **52**, 193-231.
- 6 A. J. Nozik, *Phys. E (Amsterdam, Neth.)*, 2002, **14**, 115-120.
- 7 M. C. Beard and R. J. Ellingson, *Laser Photonics Rev.*, 2008, **2**, 377-399.
- 8 M. C. Beard, A. G. Midgett, M. C. Hanna, J. M. Luther, B. K. Hughes and A. J. Nozik, *Nano Lett.*, 2010, **10**, 3019-3027.
- 9 C. S. Sandeep, S. t. Cate, J. M. Schins, T. J. Savenije, Y. Liu, M. Law, S. Kinge, A. J. Houtepen and L. D. A. Siebbeles, *Nat. Commun.*, 2013, **4**, 2360.
- 10 J. B. Sambur, T. Novet and B. A. Parkinson, *Science*, 2010, **330**, 63-66.
- 11 W. A. Tisdale, K. J. Williams, B. A. Timp, D. J. Norris, E. S. Aydil and X. Y. Zhu, *Science*, 2010, **328**, 1543-1547.
- 12 M. V. Kovalenko, L. Manna, A. Cabot, Z. Hens, D. V. Talapin, C. R. Kagan, V. I. Klimov, A. L. Rogach, P. Reiss, D. J. Milliron, F. Guyot-Sionnest, G. Konstantatos, W. J. Parak, T. Hyeon, B. A. Korgel, C. B. Murray and W. Heiss, *Acs Nano*, 2015, **9**, 1011-1057.
- 13 Y. Liu, M. Gibbs, J. Puthussery, S. Gaik, R. Ihly, H. W. Hillhouse and M. Law, *Nano Lett.*, 2010, **10**, 1960-1969.
- 14 J. M. Luther, M. Law, Q. Song, C. L. Perkins, M. C. Beard and A. J. Nozik, *Acs Nano*, 2008, **2**, 271-280.
- 15 M. V. Kovalenko, M. Scheele and D. V. Talapin, *Science*, 2009, **324**, 1417-1420.
- 16 D. V. Talapin and C. B. Murray, *Science*, 2005, **310**, 86-89.
- 17 E. Talgorn, Y. Gao, M. Aerts, L. T. Kunneman, J. M. Schins, T. J. Savenije, M. A. van Huis, H. S. J. van der Zant, A. J. Houtepen and L. D. A. Siebbeles, *Nat. Nanotechnol.*, 2011, **6**, 733-739.
- 18 Y. Liu, J. Tolentino, M. Gibbs, R. Ihly, C. L. Perkins, Y. Liu, F. Crawford, J. C. Hemminger and M. Law, *Nano Lett.*, 2013, **13**, 1578-1587.
- 19 F. Hetsch, N. Zhao, S. V. Kershaw and A. L. Rogach, *Mater. Today*, 2013, **16**, 312-325.
- 20 B. Ding, Y. Wang, P.-S. Huang, D. H. Waldeck and J.-K. Lee, *J. Phys. Chem. C*, 2014, **118**, 14749-14758.
- 21 S. J. Baik, K. Kim, K. S. Lim, S. Jung, Y.-C. Park, D. G. Han, S. Lim, S. Yoo and S. Jeong, *J. Phys. Chem. C*, 2011, **115**, 607-612.
- 22 M. A. van Huis, L. T. Kunneman, K. Overgaag, Q. Xu, G. Pandraud, H. W. Zandbergen and D. Vanmaekelbergh, *Nano Lett.*, 2008, **8**, 3959-3963.
- 23 G. S. Shanker, A. Swarnkar, A. Chatterjee, S. Chakraborty, M. Phukan, N. Parveen, K. Biswas and A. Nag, *Nanoscale*, 2015, **7**, 9204-9214.

- 24 D. V. Talapin, J.-S. Lee, M. V. Kovalenko and E. V. Shevchenko, *Chem. Rev.*, 2010, **110**, 389-458.
- 25 A. H. Ip, S. M. Thon, S. Hoogland, O. Voznyy, D. Zhitomirsky, R. Debnath, L. Levina, L. R. Rollny, G. H. Carey, A. Fischer, K. W. Kemp, I. J. Kramer, Z. J. Ning, A. J. Labelle, K. W. Chou, A. Amassian and E. H. Sargent, *Nat. Nanotechnol.*, 2012, **7**, 577-582.
- 26 D. Zhitomirsky, I. J. Kramer, A. J. Labelle, A. Fischer, R. Debnath, J. Pan, O. M. Bakr and E. H. Sargent, *Nano Lett.*, 2012, **12**, 1007-1012.
- 27 G. H. Carey, I. J. Kramer, P. Kanjanaboos, G. Moreno-Bautista, O. Voznyy, L. Rollny, J. A. Tang, S. Hoogland and E. H. Sargent, *Acs Nano*, 2014, **8**, 11763-11769.
- 28 S. M. Thon, A. H. Ip, O. Voznyy, L. Levina, K. W. Kemp, G. H. Carey, S. Masala and E. H. Sargent, *ACS Nano*, 2013, **7**, 7680-7688.
- 29 C.-H. M. Chuang, P. R. Brown, V. Bulović and M. G. Bawendi, *Nat. Mater.*, 2014, **13**, 796-801.
- 30 Z. J. Ning, O. Voznyy, J. Pan, S. Hoogland, V. Adinolfi, J. X. Xu, M. Li, A. R. Kirmani, J. P. Sun, J. Minor, K. W. Kemp, H. P. Dong, L. Rollny, A. Labelle, G. Carey, B. Sutherland, I. Hill, A. Amassian, H. Liu, J. Tang, O. M. Bakr and E. H. Sargent, *Nat. Mater.*, 2014, **13**, 822-828.
- 31 K. S. Jeong, J. Tang, H. Liu, J. Kim, A. W. Schaefer, K. Kemp, L. Levina, X. H. Wang, S. Hoogland, R. Debnath, L. Brzozowski, E. H. Sargent and J. B. Asbury, *ACS Nano*, 2012, **6**, 89-99.
- 32 J. Tang, K. W. Kemp, S. Hoogland, K. S. Jeong, H. Liu, L. Levina, M. Furukawa, X. H. Wang, R. Debnath, D. K. Cha, K. W. Chou, A. Fischer, A. Amassian, J. B. Asbury and E. H. Sargent, *Nat. Mater.*, 2011, **10**, 765-771.
- 33 D. N. Dirin, S. Dreyfuss, M. I. Bodnarchuk, G. Nedelcu, P. Papagiorgis, G. Itkos and M. V. Kovalenko, *J. Am. Chem. Soc.*, 2014, **136**, 6550-6553.
- 34 R. W. Crisp, D. M. Kroupa, A. R. Marshall, E. M. Miller, J. B. Zhang, M. C. Beard and J. M. Luther, *Sci. Rep.*, 2015, **5**.
- 35 B. K. Hughes, D. A. Ruddy, J. L. Blackburn, D. K. Smith, M. R. Bergren, A. J. Nozik, J. C. Johnson and M. C. Beard, *Acs Nano*, 2012, **6**, 5498-5506.
- 36 Y. Gai, H. Peng and J. Li, *J. Phys. Chem. C*, 2009, **113**, 21506-21511.
- 37 A. Franceschetti, *Phys. Rev. B*, 2008, **78**, 075418.
- 38 D. Kim, D.-H. Kim, J.-H. Lee and J. C. Grossman, *Phys. Rev. Lett.*, 2013, **110**, 196802.
- 39 S. J. Oh, N. E. Berry, J.-H. Choi, E. A. Gaulding, T. Paik, S.-H. Hong, C. B. Murray and C. R. Kagan, *ACS Nano*, 2013, **7**, 2413-2421.
- 40 S. J. Oh, N. E. Berry, J.-H. Choi, E. A. Gaulding, H. Lin, T. Paik, B. T. Diroll, S. Muramoto, C. B. Murray and C. R. Kagan, *Nano Lett.*, 2014, **14**, 1559-1566.
- 41 H. Wang, I. Barceló, T. Lana-Villarreal, R. Gómez, M. Bonn and E. Cánovas, *Nano Lett.*, 2014, **14**, 5780-5786.
- 42 H. Choi, J.-H. Ko, Y.-H. Kim and S. Jeong, *J. Am. Chem. Soc.*, 2013, **135**, 5278-5281.
- 43 C. R. Bealing, W. J. Baumgardner, J. J. Choi, T. Hanrath and R. G. Hennig, *ACS Nano*, 2012, **6**, 2118-2127.
- 44 A. P. Kaushik, B. Lukose and P. Clancy, *Acs Nano*, 2014, **8**, 2302-2317.
- 45 C. Fang, M. A. van Huis, D. Vanmaekelbergh and H. W. Zandbergen, *Acs Nano*, 2009, **4**, 211-218.
- 46 K. Kimura, K. Nakajima, Y. Fujii and M. Mannami, *Surf. Sci.*, 1994, **318**, 363-367.
- 47 O. Voznyy, S. M. Thon, A. H. Ip and E. H. Sargent, *J. Phys. Chem. Lett.*, 2013, **4**, 987-992.
- 48 M. J. Fernee, E. Thomsen, P. Jensen and H. Rubinsztein-Dunlop, *Nanotechnology*, 2006, **17**, 956-962.
- 49 J. Gao and J. C. Johnson, *Acs Nano*, 2012, **6**, 3292-3303.
- 50 C. A. Nelson and X. Y. Zhu, *J. Am. Chem. Soc.*, 2012, **134**, 7592-7595.
- 51 D. Bozyigit, S. Volk, O. Yarema and V. Wood, *Nano Lett.*, 2013, **13**, 5284-5288.
- 52 P. Nagpal and V. I. Klimov, *Nat. Commun.*, 2011, **2**, 486.
- 53 B. Diaconescu, L. A. Padilha, P. Nagpal, B. S. Swartzentruber and V. I. Klimov, *Phys. Rev. Lett.*, 2013, **110**, 127406.
- 54 Y. Zhang, D. Zherebetsky, N. D. Bronstein, S. Barja, L. Lichtenstein, D. Schuppisser, L.-W. Wang, A. P. Alivisatos and M. Salmeron, *Nano Lett.*, 2015, **15**, 3249-3253.
- 55 J. D. Hackley, D. A. Kislitsyn, D. K. Beaman, S. Ulrich and G. V. Nazin, *Rev. Sci. Instrum.*, 2014, **85**, 103704.
- 56 D. A. Kislitsyn, C. F. Gervasi, T. Allen, P. K. B. Palomaki, J. D. Hackley, R. Maruyama and G. V. Nazin, *J. Phys. Chem. Lett.*, 2014, **5**, 3701-3707.
- 57 S. V. Kilina, C. F. Craig, D. S. Kilin and O. V. Prezhdo, *J. Phys. Chem. C*, 2007, **111**, 4871-4878.
- 58 S. V. Kilina, D. S. Kilin and O. V. Prezhdo, *ACS Nano*, 2008, **3**, 99-99.
- 59 Z. Hens, D. Vanmaekelbergh, E. Stoffels and H. van Kempen, *Phys. Rev. Lett.*, 2002, **88**, 236803.
- 60 Z. Hens, E. S. Kooij, G. Allan, B. Grandidier and D. Vanmaekelbergh, *Nanotechnology*, 2005, **16**, 339-343.
- 61 J. Yang, H. I. Elim, Q. Zhang, J. Y. Lee and W. Ji, *J. Am. Chem. Soc.*, 2006, **128**, 11921-11926.
- 62 C. J. Chen, *Introduction to Scanning Tunneling Microscopy*, Oxford University Press, New York, Second Edition edn., 2008.
- 63 U. Banin, Y. W. Cao, D. Katz and O. Millo, *Nature*, 1999, **400**, 542-544.
- 64 L. Jdira, P. Liljeroth, E. Stoffels, D. Vanmaekelbergh and S. Speller, *Phys. Rev. B*, 2006, **73**.
- 65 I. Moreels, K. Lambert, D. Smeets, D. De Muynck, T. Nollet, J. C. Martins, F. Vanhaecke, A. Vantomme, C. Delerue, G. Allan and Z. Hens, *Acs Nano*, 2009, **3**, 3023-3030.
- 66 W. Lee, N. P. Dasgupta, H. J. Jung, J. R. Lee, R. Sinclair and F. B. Prinz, *Nanotechnology*, 2010, **21**.
- 67 N. P. Dasgupta, W. Lee and F. B. Prinz, *Chem. Mater.*, 2009, **21**, 3973-3978.
- 68 T. D. Krauss, F. W. Wise and D. B. Tanner, *Phys. Rev. Lett.*, 1996, **76**, 1376-1379.
- 69 Z. X. Sun, I. Swart, C. Delerue, D. Vanmaekelbergh and P. Liljeroth, *Phys. Rev. Lett.*, 2009, **102**, 196401.
- 70 N. Nilius, T. M. Wallis and W. Ho, *Science*, 2002, **297**, 1853-1856.
- 71 S. Fölsch, P. Hyldgaard, R. Koch and K. H. Ploog, *Phys. Rev. Lett.*, 2004, **92**, 056803.
- 72 S. Fölsch, J. Yang, C. Nacci and K. Kanisawa, *Phys. Rev. Lett.*, 2009, **103**, 096104.
- 73 I. Moreels, Y. Justo, B. De Geyter, K. Haustraete, J. C. Martins and Z. Hens, *Acs Nano*, 2011, **5**, 2004-2012.
- 74 S. Kilina, S. Ivanov and S. Tretiak, *J. Am. Chem. Soc.*, 2009, **131**, 7717-7726.
- 75 J. T. Margraf, A. Ruland, V. Sgobba, D. M. Guldi and T. Clark, *Langmuir*, 2013, **29**, 15450-15456.
- 76 I. Horcas, F. Fernández, J. M. Gómez-Rodríguez, J. Colchero, J. Gómez-Herrero and A. M. Baro, *Rev. Sci. Instrum.*, 2007, **78**, 2432410.